

1 Icequake-magnitude scaling relationship along a rift within the Ross 2 Ice Shelf, Antarctica

3 Mong-Han Huang¹, Kathrine Udell Lopez¹, Kira G. Olsen^{1,2}

4 ¹Department of Geology, University of Maryland, College Park, MD, USA

5 ²NASA Goddard Space Flight Center, Greenbelt, MD, USA

6

7 **Abstract**

8 Fractures within ice shelves are zones of weakness, which can deform on timescales from
9 seconds to decades. Icequakes produced during the fracturing process show a higher *b-value* in
10 the Gutenberg-Richter scaling relationship than continental earthquakes. We investigate
11 icequakes on the east side of rift WR4 in the Ross Ice Shelf, Antarctica. Our model suggests a
12 maximum icequake slip depth that is ~7.8 m below rift surface, where the slip area can only
13 grow laterally along the fracture planes. We propose ductile deformation below this depth,
14 potentially due to saturation of unfrozen water. We use remote sensing and geodetic tools to
15 quantify surface movement on different time scales and find that the majority of icequakes
16 occurred during falling tides. The total seismic moment is < 1% of the estimated geodetic
17 moment during a tidal cycle. This study demonstrates the feasibility of using seismology and
18 geodesy to investigate ice rift zone rheology.

19

20 **Plain Language Summary**

21 Fractures located on ice shelves are weak compared to the rest of the ice shelf. They deform
22 over seconds to decades, and icequakes can be accompanied by their deformation. We find
23 that tides, particularly falling tides, influence the frequency of icequake occurrence the most. We
24 also find that small magnitude icequakes are a larger proportion of total icequakes when
25 compared to the proportion of small magnitude continental earthquakes in relation to total global
26 earthquakes. We test whether this proportion is due to the maximum depth estimated at 7.8 m
27 below the surface of the rift zone by using satellite imagery, Global Navigation Satellite Systems
28 (GNSS) measurements, and a seismometer located near a fracture on the Ross Ice Shelf. We
29 propose that the rift zone below 7.8 m depth behaves as ductile deformation possibly due to
30 saturation with unfrozen water, whereas the region above this depth is more prone to brittle
31 fracture that can generate icequakes.

32

33 **Key points:**

- 34 1. Along the rift WR4 in the Ross Ice Shelf, evidence suggests most icequakes are driven
35 by falling tides than long-term rift opening.
36 2. The b-value of icequakes in the Gutenberg-Richter relationship is generally greater than
37 that for continental earthquakes.
38 3. We propose that the rift is water saturated ~7.8 m below the rift surface and prevents
39 icequakes from occurring below this depth.

40

41 **1. Introduction**

42 The Gutenberg-Richter (G-R) relationship describes a relationship between the number of
43 earthquakes in a region greater than a certain magnitude and that magnitude (*Gutenberg and
44 Richter, 1956*). This relationship can be represented as:

45

$$46 \log_{10} N = a - bM_W, \quad (1)$$

47

48 where a represents the number of earthquakes when the moment magnitude (M_W) = 0, and b is
49 the slope of the scaling relationship. For instance, when $b = 1$, there are $10^1 = 10$ times more
50 seismic events at a given magnitude than at the next lower magnitude value. On average, the b -
51 value of global earthquakes is ~ 1 (*Lay and Wallace, 1995*), but for slow slip events and active
52 volcanic regions, the b -value is close to 1.5 (*Ide et al., 2007; Gombert et al., 2016; Rundle,
53 1989*). From global seismicity, the b -value appears to be around 1.5 for $M_W > \sim 7 - 7.5$ (*Pacheco
54 et al., 1992*). The break in the relationship is thought to be due to a presence of a “brittle-ductile
55 transition zone”, a depth which slip cannot penetrate through, and therefore the slip area can
56 only grow laterally.

57

58 The Ross Ice Shelf in Antarctica is the largest ice shelf on Earth ($\sim 525,000 \text{ km}^2$; Figure 1a,b).
59 The ice shelf is a few hundred to over 1,000 meters thick and is moving toward the ocean with a
60 speed from approximately 400 to 1,090 m/yr (ITS_LIVE dataset, *Gardner et al., 2019*). About
61 170 km north from the grounding line, several rifts have been mapped within the Ross Ice Shelf
62 (Figure 1b; *Walker et al., 2013; Walker and Gardner, 2019*). Along Western Ross rift 4, or WR4,
63 (Figure 1b,c), the ice velocities of the landward and seaward sides of the rift are different,
64 causing a 10 - 50 m opening of the rift annually (*Walker and Gardner, 2019*). Using seismic data
65 collected at station DR14 near WR4 between 2014 and 2016, *Olsen et al. (2021)* detected
66 $\sim 13,000$ icequakes during a 25-month period. Among these icequakes, they were able to

67 determine the magnitudes for ~2,500 icequakes. Based on the timing of the icequakes, they
68 found a clear positive correlation between the onset of icequakes and tidally driven tensile
69 stress, which is consistent with previous studies in a broader region on Ross Ice Shelf (e.g.
70 *Olinger et al.*, 2019; *Chen et al.*, 2019). The G-R relationship within the rift zone shows a b-
71 value between 1.2 and 1.5 (*Olinger et al.*, 2019; *Olsen et al.*, 2021), which is greater than similar
72 magnitude continental earthquakes.

73
74 In this study, we investigate the higher b-value within WR4, estimate the energy required for the
75 long-term rift zone opening, and compare the estimate with the cumulative seismic moment
76 from the icequakes catalog created by *Olsen et al.* (2021). To accomplish this, we use both
77 satellite imagery and Global Navigation Satellite System (GNSS) data to measure long-term
78 surface strain rate and displacement during tidal cycles. We propose a maximum depth of
79 icequakes within WR4 and a constant slip when the magnitude is greater than a certain value.
80 This simple model can explain the higher b-value and predicts a reasonable slip value as well
81 as stress drop. This work highlights the value of combining both seismologic and geodetic
82 datasets for understanding Earth's polar ice sheets as well as icy worlds.

83

84 **2. Data and Methods**

85 **2.1 Seismic Data**

86 The seismic catalog used in this study was recently published by *Olsen et al.* (2021). The data
87 was collected by a temporary seismic deployment spanning the Ross Ice Shelf during a 34-
88 station campaign RIS/DRRIS project between November 2014 and December 2016 (*Bromirski*
89 *et al.*, 2015). *Olsen et al.* (2021) calculated the azimuth of 2,509 icequakes recorded at seismic
90 station DR14 using surface-wave-arrival back azimuth method proposed by *Baker and Stevens*
91 (2004). This method analyzes the polarization of recorded Rayleigh waves for back azimuth
92 estimation using a single seismic station. To estimate distances between seismic station DR14
93 and icequake epicenters we handpicked the P and Rayleigh wave arrival times for these
94 icequakes, then combined azimuth and distance calculations to locate this set of icequakes
95 (Figure 2). The local magnitude (M_L) of each icequake was calculated using the maximum
96 absolute displacement amplitude of each event, as described in *Olsen et al.* (2021).

97

98 **2.2 Satellite Imagery & GNSS Data**

99 To investigate long-term velocity and deformation on the Ross Ice Shelf, we adopt the horizontal
100 movement and opening of WR4 estimated by *Walker and Gardner* (2019). We also use the

101 *ITS_LIVE* dataset to calculate surface strain rate near WR4 (Supplementary Text S1). This is an
102 ice shelf surface velocity measurement based on satellite data (*Gardner et al.*, 2019). For short-
103 term (diurnal) deformation, we use GNSS data to measure inter-tidal cycle displacements.
104 Thirteen GNSS stations were temporarily deployed on the Ross Ice Shelf between November
105 2015 and early 2017 (*Bromirski and Gerstoft*, 2017). *Klein et al.* (2020) processed the high-rate
106 (1-Hz) GNSS solutions from the 13 stations and characterized both short-term (sub-daily) and
107 long-term (annual) displacements. Stations DR14 and DR10 are located on each side of WR4,
108 with DR14 ~2 km and DR10 ~10 km away from WR4 (Figure 1b,c). DR10 has 2 years of
109 continuous displacement measurements, whereas there is a data gap for DR14 during the
110 winter season due to a lack of sunlight.

111

112 **3. Results**

113 **3.1 Seismic Results**

114 From the spatial distribution of the icequakes, there is a clear cluster of seismicity located along
115 a bent segment of WR4 (Figure 2a). This bent segment is ~460 m in length and ~160 m in width
116 (Figure S1). Although the uncertainty of icequake locations is high due to a single-station
117 location technique, this result strongly suggests that the majority of located icequakes in this
118 catalog occurred within the bend inside the rift zone. This finding is consistent with icequake
119 locations at WR4 calculated by *Olinger et al.* (2019) using a multi-station location technique.

120

121 We find a clear increase in the minimum magnitude of icequake detection with distance from
122 seismic station DR14 (Figure S2). For example, the minimum detection is approximately M_W -2
123 on the near side of WR4 relative to DR14, and M_W -1.2 on the far side. Although the icequake
124 locations are not well constrained, there is a clear cluster of seismicity between 2 and 4 km
125 possibly coming from the rift zone (Figure 2a,b). To fully capture the G-R relationship of the rift
126 zone, we only consider icequakes within 4 km of distance from DR14. We also change the
127 minimum magnitude cutoff until the icequake population density distribution becomes uniform,
128 which is when $M_W > -1$ (Figure 2b). The G-R relationship from this subset of icequakes shows a
129 clear change of slope when $M_W = -0.4$ (Figure 2c). Using a least square fit to the curves, the b-
130 value is 1.1 between M_W -1 and -0.4, and 2.0 between M_W -0.4 and 0.3. We do not include M_W
131 0.4 in this calculation because there is only one icequake in this magnitude, which may not be
132 representative of the distribution. We additionally plot the icequake G-R relationship of the near-
133 and far-sides of WR4 and find consistent change of b-value at M_W -0.4 (Figure S3a).

134

135 **3.2 Long-term (annual) deformation**

136 *Walker and Gardner* (2019) found a rift opening rate between 10 and 50 m/yr along WR4. At the
137 bent segment of WR4 (Figure 2a), the opening rate is ~10 m/yr. Since the width of WR4 here is
138 160 m, this bent segment opens ~6% per year. We calculated the principal strain rates and
139 dilatation rate from the strain rate tensor on 500 m spacing grid points at WR4 (Figures 3a &
140 S5). The result shows that the principal extension strain rate axes align perpendicular to the
141 strike of WR4, even along the bent segment of WR4, implying low to negligible shear motion
142 along the rift during long-term deformation (Figures 3a & S5).

143

144 **3.3 Short-term (diurnal) deformation**

145 GNSS stations DR10 and DR14 are collocated with the seismic stations (*Bromirski et al.*, 2015;
146 *Bromirski and Gerstoft*, 2017). We adopt the displacement time series solutions from *Klein et al.*
147 (2020). In a 20-day time window of one GNSS station, there is up to 0.5 m vertical displacement
148 during diurnal tidal cycles (U-D in Figure 3b). In horizontal components, after removing the long-
149 term trends, we find up to 0.4 m horizontal displacements during tidal cycles (E-W and N-S in
150 Figure 3b). Although we are not able to directly estimate deformation within the rift, if we
151 assume rigid motion of the ice shelf (i.e. negligible internal deformation), the majority of the
152 internal deformation would occur within the rifts. We can therefore estimate the internal strain of
153 WR4 near the bent segment by taking the differential displacement between DR10 and DR14,
154 which is similar to the approach for the Nascent Iceberg also on Ross Ice Shelf (*Hurford and*
155 *Brunt*, 2014). As shown in Figure 3c, the results indicate up to 0.015 m in horizontal and 0.03 m
156 in vertical displacements with 60-sample moving average. Note that positive displacement in the
157 north-south direction shows an increase in distance between the two GNSS stations during
158 falling tides. The majority of the icequakes (vertical lines in Figure 3c) occurred during falling
159 tides and is consistent with tidal patterns identified in *Olsen et al.* (2021).

160

161 **4. Discussion**

162 **4.1 Energy budget associated with icequakes, long- and short-terms deformation**

163 **4.1.1 Seismic moment**

164 We calculated the cumulative seismic moment based on the icequake catalog derived by *Olsen*
165 *et al.* (2021). The scaling between M_L and M_W in *Olsen et al.* (2021) is based on *Munafò et al.*
166 (2016) for small earthquakes (local magnitude $M_L < 3$):

167

168
$$M_W = \frac{2}{3} M_L + 1.15. \quad (2)$$

169

170 Following this, moment magnitude (M_W) is related to the seismic moment (M_o) (*Hanks and*
171 *Kanamori, 1979*):

172

$$173 \quad M_W = \frac{2}{3} \log_{10} M_o - 6.07, \quad (3)$$

174

175 where M_o is in the unit of N m. Comparing Equations 2 with 3, it suggests that M_L can directly
176 scale with seismic moment for lower magnitude events when the instrument cutoff frequency is
177 much lower than the corner frequency of the event (*Deichmann, 2017*). Although the scaling
178 relationship is slightly different, similar results were found in Southern California (*Ross et al.,*
179 *2016; Staudenmaier et al., 2018*) and Switzerland (*Bethmann et al., 2011*). The cumulative
180 seismic moment (Figure 4a) shows a significant seismic moment increase due to the largest M_W
181 1.5 event. If we remove the largest event for simple visual illustration, we find a clear difference
182 in accumulation during summer and winter, where greater seismic moment accumulation is
183 observed during austral wintertime (March-September). A plot of cumulative number of
184 icequakes with time shows a similar pattern (Figure S3b). This result is consistent with the
185 finding by *Olinger et al. (2019)* and *Chen et al. (2019)*.

186

187 **4.1.2 Long-term strain energy**

188 To estimate the strain energy within the bent segment of the rift, we first determine the volume
189 of the rift and the stress within the material. From visual inspection of the icequake locations
190 (Figure 2a), it is reasonable to assume that the majority of the icequakes are from the bent
191 segment of the rift. The thickness of the Ross Ice Shelf near WR4 is estimated to be ~300 m
192 using shallow-ice radar echogram images (ROSETTA-Ice project; *Das et al., 2020*). Assuming
193 isostasy and the density of water = 1,030 kg/m³ and ice = 917 kg/m³, and the surface
194 topography of the rift zone is ~20 m below the rest of the ice shelf (from the 2 m resolution
195 digital elevation model [DEM] of the Worldview satellite imagery; Figure S1), the thickness of the
196 rift zone is estimated as ~118 m. As a result, the volume of the bent segment is estimated as
197 $8.7 \times 10^6 \text{ m}^3$.

198

199 As described in Section 3.2, the long-term dilation rate is ~0.063/yr. The amount of stress
200 required to maintain this dilation rate is estimated to be $\sim 2 \times 10^5 \text{ Pa}$, using a power-law relation
201 between steady-state strain rate and deviatoric stress for Ross Ice Shelf (*Jezek et al., 1985*).
202 Assuming uniform strain rate within the rift, the annual strain energy is estimated as,

203

204

$$U = \frac{1}{2} V \sigma \dot{\epsilon} = 8.8 \times 10^7 Nm/yr, \quad (4)$$

205

206 where V is volume, σ is tensile stress required for the amount of strain rate, and $\dot{\epsilon}$ is strain rate.

207 This annual accumulated strain energy is equivalent to a M_W -0.77 event per day (orange line in

208 Figure 4a). This amount of strain energy rate is clearly lower than observed seismic moment

209 rate (blue line in Figure 4a). The observed icequakes are unlikely triggered by the long-term

210 dilatation of the rift.

211

212 **4.1.3 Short-term (Diurnal) tidal stress**

213 As shown in Figure 3c, there is up to a few centimeters of displacement between stations DR10

214 and DR14. If we assume that deformation is within the rift, the peak vertical displacement shown

215 in Figure 3c within the bent segment of WR4 is ~ 0.03 m during falling tide. As the tidal cycle is

216 diurnal, which is significantly shorter than the Maxwell relaxation time of ice ($\sim 10^8$ seconds), we

217 assume elastic deformation in one tidal cycle. If we also assume slip (d) is the same across the

218 entire rift wall, the slip area (A) as the length of the bent segment \times thickness of WR4 $\approx 48,700$

219 m^2 , and the shear modulus (μ) of ice as 3.6×10^9 Pa (Vaughan *et al.*, 2016), the geodetic

220 moment (M_{Go}) is: $M_{Go} = \mu A d = \sim 5.8 \times 10^{12}$ N m (or M_W 2.4) every falling tidal. The largest

221 observed icequake within the rift (M_W 0.4; Figure 2b,c) is only 0.09% of M_{Go} . This result

222 suggests that the seismic moment observed here only represents small but routinely fracturing

223 events on a small portion of the rift wall.

224

225 **4.2 G-R scaling relationship of icequakes at WR4**

226 To explore the b-value in the G-R relationship, we first discuss seismic moment and earthquake

227 scaling. The seismic moment (M_o) is a measurement of the energy release of an event:

228

229

$$M_o = \mu A d. \quad (5)$$

230

231 Note Equation 5 has the same form as the geodetic moment. If μ of ice is constant, M_W scales

232 with both A and d . As slip and slip area grow, d and A grow as a function of length (l) and

233 length-square (l^2), respectively. As a result, when a length scale increases by an order for d and

234 A , seismic moment (M_o) increases by 3 orders and M_W increases by a factor of two (Equation 3).

235

236 If there is a total area (S) that allows any slip to occur within S , the probability of an event with a
 237 certain slip area decreases with a larger event size as,

238
 239
$$N_i = \frac{S}{A_i}, \quad (6)$$

240
 241 where N_i is the number of events that can occur with a given slip area A_i . As a result, N_i and A_i
 242 are inversely proportional to each other, suggesting $N_i \propto l^{-2}$. Relating Equations 1, 3, and 5:

243 $\log_{10} N = a - b[\frac{2}{3} \log_{10}(\mu A d) - 6.07]$, and therefore:

244
 245
$$b \propto -\frac{3}{2} \frac{\log_{10} N}{\log_{10} A d}. \quad (7)$$

246
 247 Since $N_i \propto l^{-2}$, $A \propto l^2$, and $d \propto l$, $b = 1$.

248
 249 Next, if there is a maximum depth (W_o) from ground surface where slip cannot penetrate
 250 through, slip area is represented as: $A = W_o L$, where L is the lateral length scale of fault. This
 251 implies $A \propto l$. If $d \propto l$, Equation 7 suggests that $b = 0.75$. Alternatively, *Romanowicz and Rundle*
 252 (1993) suggested that d could be invariant ($d \propto l^0$) when slip area reached W_o , and therefore $b =$
 253 1.5. The G-R relationship of icequakes within the bent segment of WR4 indicates two b-values
 254 when $M_W > -1$ (Figure 2b). When M_W is between -1 and -0.4 the b-value is close to 1 and when
 255 $M_W > -0.4$, $b \approx 2$. Although the observed b-value is greater than 1.5, this pattern indicates a
 256 change of scaling relationship when $M_W \approx -0.4$ and implies that the icequake slip area reaches
 257 the maximum depth W_o when $M_W > -0.4$.

258
 259 Stress drop ($\Delta\sigma$) is a change of shear stress due to a seismic event. Stress drop can be
 260 influenced by shear modulus (μ), slip area (A), and slip (d):

261
 262
$$\Delta\sigma = C \mu \frac{d}{\sqrt{A}}, \quad (8)$$

263
 264 where $C = \sqrt{5}$ for a rectangular slip area (*Pacheco et al.*, 1992), and $C = \frac{7\pi}{16}$ for a circular slip
 265 area (*Lay and Wallace*, 1995). From Equation 8, stress drop is a constant between different
 266 magnitudes when $b = 1$ (i.e. $A \propto l^2$ and $d \propto l$). If slip (d_o) is invariant ($d \propto l^2$) and slip area scales
 267 only with fault length ($A \propto l$), $\Delta\sigma$ scaling becomes:

268

269

$$\Delta\sigma = C \mu \frac{d_o}{\sqrt{W_o L}} \propto l^{-1/2}. \quad (9)$$

270

271 This means stress drop decreases as fault length (and moment magnitude) increases.

272

273 **4.3 Predicted slip and slip area of the largest event**

274 The seismic moment of the largest icequake within the rift (M_W 0.4) is 5×10^9 N m. From

275 Equation 5 and $\mu = 3.6 \times 10^9$ Pa, the slip and slip area product, $A d = 1.4 \text{ m}^3$. If we assume that

276 the largest icequake has a slip equivalent to the largest differential displacement recorded by

277 GNSS stations ($d = 0.05$ m; Figure 3c), then $A = 28 \text{ m}^2$. If we also assume the largest icequake

278 corresponds to the slip of the entire bent segment (460 m; Figure 2a), then the width of the slip

279 (in vertical direction) is area divided by length: $W_o = \frac{A}{L} = 0.6$ m. We can then estimate the stress

280 drop ($\Delta\sigma$) of this event, as $\Delta\sigma = \sqrt{5} \mu \frac{d}{\sqrt{A}} = 76$ MPa. This value, however, is much greater than

281 the tensile strength of ice estimated as 1.5 MPa, (*Podolskiy and Walter, 2016*), or 1.43 MPa

282 within the temperature range -10 to -20°C (*Petrovic, 2003*). As a result, the amount of slip for

283 this M_W 0.4 event is likely to be smaller than 0.05 m. From the G-R relationship (Figure 2b), if

284 we consider the change of b-value as the critical condition when slip area cannot grow deeper,

285 we can then assume that $\Delta\sigma = 1.5$ MPa at M_W -0.4. In this scenario, $d \approx 0.0015$ m and $A \approx 61$

286 m^2 . This suggests a $7.8 \text{ m} \times 7.8 \text{ m}$ slip area.

287

288 Based on the analysis described above, we propose a depth similar to the “brittle-ductile

289 transition” concept for Earth’s crust. As shown in Figure 4b, for the Ross Ice Shelf this depth

290 indicates a maximum depth where brittle failure could occur. Assuming the thickness of ice

291 within the rift zone is ~ 118 m, as estimated in Section 4.1.2, this maximum brittle deformation

292 depth is $\sim 6.6\%$ of the rift. This also suggests that the fault length of the largest M_W 0.4 icequake

293 within the rift has a fault length of ~ 120 m with stress drop = 0.39 MPa.

294

295 Here we discuss potential explanations of this maximum slip depth. Although the permeability of

296 ice is low (e.g. *Petrovic, 2003*), the porosity of the rift zone could be higher than the ice sheet

297 due to the continuous rift opening (~ 0.063 per year). We then assume the rift zone is water

298 saturated below sea level. By assuming isostasy, thickness of WR4 as 118 m, and the density

299 contrast between water and ice, the depth to saturation is ~ 6.1 m below the rift surface, or ~ 5.6

300 m if the porosity of WR4 is 10%. This depth is shallower than the proposed brittle-ductile

301 transition, but within the same order of magnitude. As air temperature is lower during wintertime,
302 the unfrozen water level may be deeper at that time. This would imply a deeper brittle-ductile
303 transition and allow for higher seismic production during winter months, as documented by
304 *Olinger et al. (2019)* and observed within the catalog of icequakes examined here (Figures 4a &
305 S3b).

306

307 **4.4 Limitation of the analysis and future directions**

308 High-resolution study of this rift is currently limited by instrumentation (single seismometer
309 located ~5 km of WR4) as well as a shorter observation period. The seismic record examined
310 here may not be of sufficient duration to capture a statistically representative number of higher-
311 magnitude icequakes. Future deployment of additional seismic stations on the flanks of WR4
312 would enable higher-accuracy icequake locations, and calculation of focal mechanisms for
313 larger icequakes. It would also allow for seismic verification of a maximum slip depth. Future
314 work including higher density seismic and GNSS station deployments will significantly increase
315 the detection level of icequakes, and we may even be able to measure surface displacement
316 associated with larger icequakes. For example, we predict millimeter-level slip when the
317 icequake $M_w > -0.4$. With high-rate GNSS stations deployed on both sides of the rift, they might
318 detect mm-levels of seismic slip as well as the sense of motion.

319

320 **5. Conclusions**

321 We suggest that icequakes within WR4 are due to slip during diurnal falling tides. By using a
322 combined seismic and geodetic dataset, we observe icequakes located within a bent segment
323 of rift WR4 on the Ross Ice Shelf, Antarctica. An increase in the number of icequakes and
324 cumulative seismic moment in winters implies more slip area available for icequake generation
325 due to colder temperature within the shallower part of the rift zone. Long-term strain energy due
326 to rift opening alone cannot explain the cumulative seismic moment of the icequakes. On the
327 other hand, diurnal tidal stress can provide a sufficient amount of energy to generate icequakes.
328 From the G-R relationship, we find a b-value greater than continental earthquakes. We adopt a
329 simple scaling relationship to explain this high b-value, which suggests an existence of a
330 maximum slip depth that is ~7.8 m below the rift surface. The proposed maximum slip is about
331 10% of the observed inter-tidal displacement between GNSS stations located on both sides of
332 WR4, and the maximum slip depth is approximately the same length scale as the estimated
333 water saturation depth of WR4.

334

335 **Acknowledgements**

336 The authors would like to thank Vedran Lekić, Nicholas Schmerr, Avinash Nayak, Victor Tsai,
337 Catherine Walker, Sophia Zipparo, and Emilie Klein for their suggestions that significantly
338 improves the quality of this work. This work is partially supported by NSF EAR-2026099 to M.-H.
339 Huang. K.G. Olsen was supported by an appointment to the NASA Postdoctoral Program at the
340 NASA Goddard Space Flight Center, administered by USRA under contract with NASA.

341

342 **Data Availability Statement**

343 The icequake catalog is included in the supplementary material and will be achieved in Zenodo
344 after the peer review process. Seismic data used in this manuscript were collected through the
345 NSF Office of Polar Programs project titled “Collaborative Research: Dynamic Response of the
346 Ross Ice Shelf to Wave-Induced Vibrations” (network code XH;
347 http://www.fdsn.org/networks/detail/XH_2014/). The GNSS data are available in *Klein et al.*,
348 2020. ITS_LIVE contains NASA products (<https://its-live.jpl.nasa.gov/>). The ROSETTA-Ice
349 product is downloaded at (<https://pgg.ideo.columbia.edu/data/rosetta-ice>). WorldView imagery
350 used in this work is available to NSF- and NASA-funded researchers via the Polar Geospatial
351 Center at the University of Minnesota.

352

353 **References**

- 354 Baker, G. E., & Stevens, J. L. (2004). Backazimuth estimation reliability using surface wave
355 polarization. *Geophysical Research Letters*, 31, L09611.
356 <https://doi.org/10.1029/2004GL019510>
- 357 Bethmann, F., Deichmann, N., Mai, & P.M. (2011), Scaling Relations of Local Magnitude versus
358 Moment Magnitude for Sequences of Similar Earthquakes in Switzerland. *Bulletin of the*
359 *Seismological Society of America*; 101, 515–534. doi:
360 <https://doi.org/10.1785/0120100179>
- 361 Bromirski, P. D., Diez, A., Gerstoft, P., Stephen, R. A., Bolmer, T., Wiens, D. A., et al. (2015).
362 Ross Ice Shelf vibrations. *Geophysical Research Letters*, 42, 7589–7597.
363 <https://doi.org/10.1002/2015GL065284>
- 364 Bromirski PD and Gerstoft P (2017) Dynamic response of the Ross Ice Shelf to wave-induced
365 vibrations 2015/2016, UNAVCO, Inc. GPS/GNSS Observations Dataset. doi:
366 10.7283/58E3-GA46.

367 Chen, Z., Bromirski, P., D, Gerstoft, P., Stephen, R. A., Lee, W. S., Yun, S., et al. (2019). Ross
368 Ice Shelf icequakes associated with ocean gravity wave activity. *Geophysical Research*
369 *Letters*, 46, 8893– 8902. <https://doi.org/10.1029/2019GL084123>

370 Das, I., Padman, L., Bell, R. E., Fricker, H. A., Tinto, K. J., Hulbe, C. L., et al. (2020).
371 Multidecadal basal melt rates and structure of the Ross Ice Shelf, Antarctica, using
372 airborne ice penetrating radar. *Journal of Geophysical Research: Earth Surface*, 125,
373 e2019JF005241. <https://doi.org/10.1029/2019JF005241>

374 Deichmann, N. (2017), Theoretical Basis for the Observed Break in ML/MW Scaling between
375 Small and Large Earthquakes. *Bulletin of the Seismological Society of America*, 107,
376 505–520. doi: <https://doi.org/10.1785/0120160318>

377 Ide, S., G. C. Beroza, D. R. Shelly, & T. Uchide (2007), A scaling law for slow earthquakes,
378 *Nature*, 447(7140), 76–79, doi:10.1038/nature05780.

379 Gardner, A. S., M. A. Fahnestock, & T. A. Scambos, 2019 [update to 2021]: ITS_LIVE Regional
380 Glacier and Ice Sheet Surface Velocities. Data archived at National Snow and Ice Data
381 Center; doi:10.5067/6II6VW8LLWJ7.

382 Gomberg, J., A. Wech, K. Creager, K. Obara, & D. Agnew (2016), Reconsidering earthquake
383 scaling, *Geophys. Res. Lett.*, 43, doi:10.1002/ 2016GL069967.

384 Gutenberg, B. & Richter, C. *Seismicity of the Earth and Associated Phenomena*, 2nd edn, 310
385 (Princeton University Press. 1956).

386 Hanks, T.C., & H. Kanamori (1979), A moment magnitude scale, *J. Geophys. Res.*, 84, 2348-
387 2350.

388 Hurford, T. A., & Brunt, K. M. (2014). Antarctic analog for dilational bands on Europa. *Earth and*
389 *Planetary Science Letters*, 401, 275–283. <https://doi.org/10.1016/j.epsl.2014.05.015>

390 Jezek, K.C., Alley, R.B., & Thomas, R.H. (1985), Rheology of glacier ice, *Science*, 227, 4692,
391 1335-1337, <https://www.jstor.org/stable/1695085>

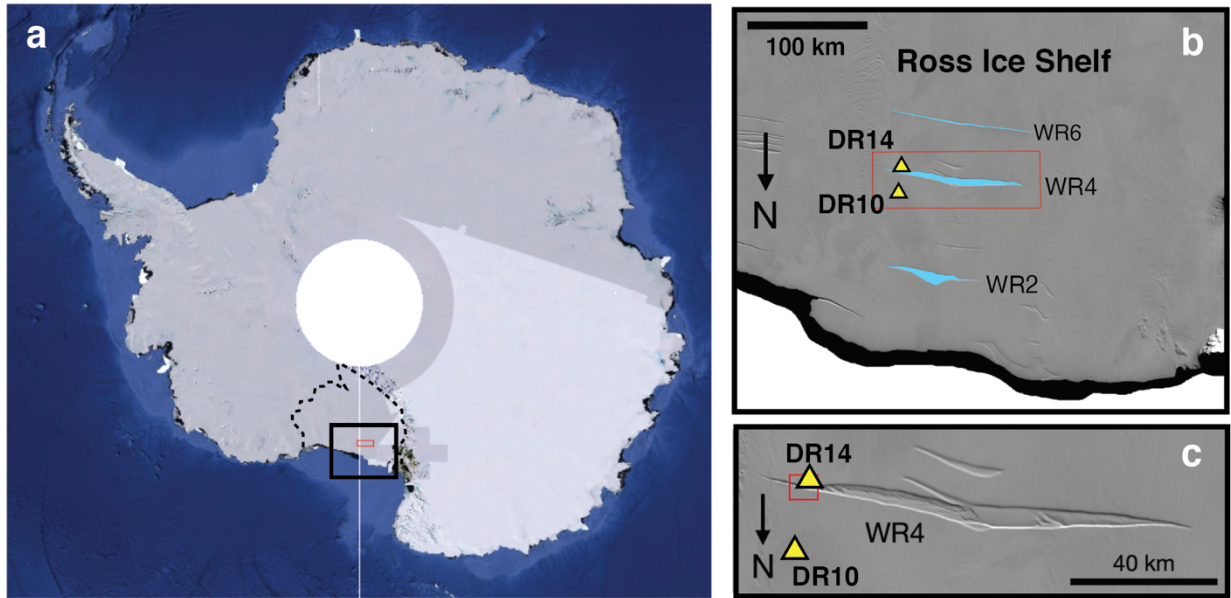
392 Klein E, Mosbeux C, Bromirski PD, Padman L, Bock Y, Springer SR, & Fricker HA (2020).
393 Annual cycle in flow of Ross Ice Shelf, Antarctica: contribution of variable basal melting.
394 *Journal of Glaciology* 66(259), 861–875. <https://doi.org/10.1017/jog.2020.61>

395 Lay, T. & Wallace, T. (1995), *Modern Global Seismology*, ISBN:012732870X, pp 521.

396 Munafò, I., Malagnini, L., & Chiaraluce, L. (2016). On the relationship between Mw and ML for
397 small earthquakes. *Bulletin of the Seismo- logical Society of America*, 106(5), 2402–
398 2408. <https://doi.org/10.1785/0120160130>

399 Olinger, S. D., Lipovsky, B. P., Wiens, D. A., Aster, R. C., Bromirski, P. D., Chen, Z., et al.
400 (2019). Tidal and thermal stresses drive seismicity along a major Ross Ice Shelf rift.
401 *Geophysical Research Letters*, 46, 6644–6652. <https://doi.org/10.1029/2019GL082842>
402 Olsen, K. G., Hurford, T. A., Schmerr, N. C., Huang, M.-H., Brunt, K. M., Zipparo, S., et al.
403 (2021). Projected Seismic Activity at the Tiger Stripe Fractures on Enceladus, Saturn,
404 from an Analog Study of Tidally Modulated Icequakes within the Ross Ice Shelf,
405 Antarctica. *Journal of Geophysical Research: Planets*, 126, e2021JE006862.
406 <https://doi.org/10.1029/2021JE006862>
407 Pacheco, J., Scholz, C. & Sykes, L. (1992). Changes in frequency–size relationship from small
408 to large earthquakes. *Nature* **355**, 71–73. <https://doi.org/10.1038/355071a0>
409 Petrovic, J.J., (2003). Mechanical properties of ice and snow, *Journal of Materials Science*, 38,
410 1-6.
411 Podolskiy, E. A., & Walter, F. (2016). Cryoseismology. *Reviews of Geophysics*, 54, 708–758.
412 <https://doi.org/10.1002/2016RG000526>
413 Romanowicz, B., & Rundle, J.B. (1993) On scaling relations for large earthquakes. *Bulletin of*
414 *the Seismological Society of America*, 83 (4): 1294–1297. doi:
415 <https://doi.org/10.1785/BSSA0830041294>
416 Ross, Z.E., Ben-Zion, Y., White, M.C., & Vernon, F.L. (2016), Analysis of earthquake body wave
417 spectra for potency and magnitude values: implications for magnitude scaling relations,
418 *Geophysical Journal International*, 207, 1158–1164, <https://doi.org/10.1093/gji/ggw327>
419 Rundle, J. B. (1989), Derivation of the complete Gutenberg-Richter magnitude-frequency
420 relation using the principle of scale invariance, *J. Geophys. Res.*, 94(B9), 12337–
421 12342, doi:[10.1029/JB094iB09p12337](https://doi.org/10.1029/JB094iB09p12337).
422 Staudenmaier, N., Tormann, T., Edwards, B., Deichmann, N., & Wiemer, S. (2018). Bilinearity in
423 the Gutenberg-Richter relation based on ML for magnitudes above and below 2, from
424 systematic magnitude assessments in Parkfield (California). *Geophysical Research*
425 *Letters*, 45, 6887–6897. <https://doi.org/10.1029/2018GL078316>
426 Vaughan, M. J., Van Wijk, K., Prior, D. J., & Bowman, M. H. (2016). Monitoring the temperature-
427 dependent elastic and anelastic proper- ties in isotropic polycrystalline ice using
428 resonant ultrasound spectroscopy. *The Cryosphere*, 10(6), 2821–2829.
429 <https://doi.org/10.5194/tc-10-2821-2016>
430 Walker, C. C., Bassis, J. N., Fricker, H. A., & Czerwinski, R. J. (2013). Structural and
431 environmental controls on Antarctic ice shelf rift propagation inferred from satellite

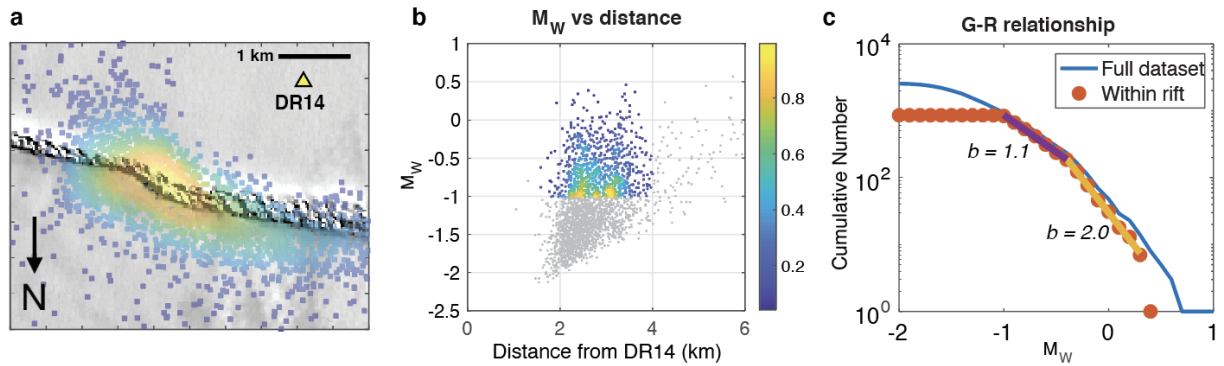
432 monitoring. *Journal of Geophysical Research: Earth Surface*, 118, 2354– 2364.
433 <https://doi.org/10.1002/2013JF002742>
434 Walker, C. C., & Gardner, A. S. (2019). Evolution of ice shelf rifts: Implications for formation
435 mechanics and morphological controls. *Earth and Planetary Science Letters*, 526,
436 115764. <https://doi.org/10.1016/j.epsl.2019.115764>
437



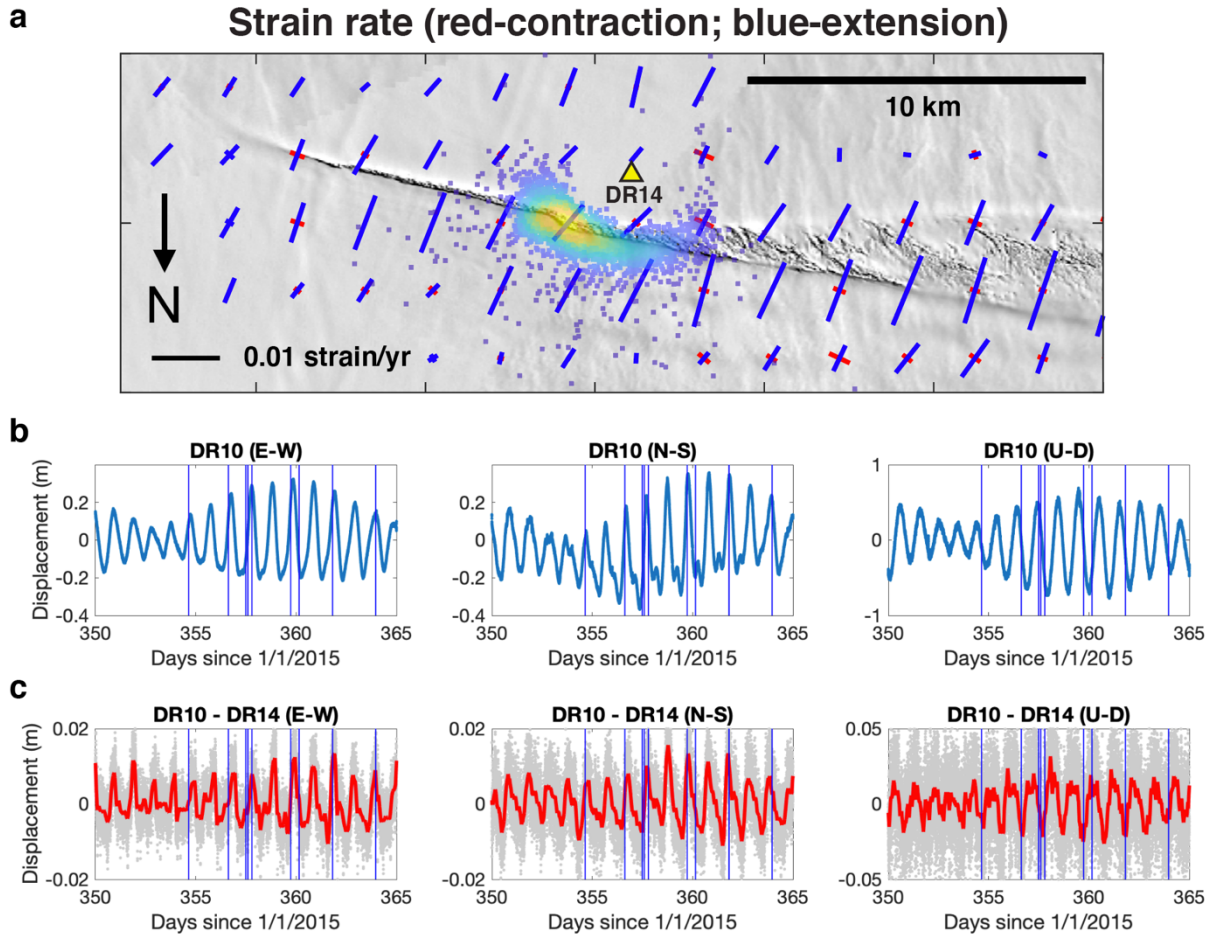
438

439 **Figure 1.** Study area. **(a)** View of Antarctica with the Antarctic Polar projection. The dashed
 440 polygon is the Ross Ice Shelf (Google Earth image) **(b)** North part of the Ross Ice Shelf. The
 441 light blue regions are the 3 major rift zones, WR2, WR4, and WR6. The yellow triangles in **b** and
 442 **c** are collocated broadband seismic and GNSS stations. The red rectangle marks the location of
 443 WR4 shown in **c**. **(c)** The red rectangle near DR14 is the figure outline of Figure 2a. The images
 444 in **b** and **c** are from MODIS.

445



446
 447 **Figure 2.** Seismicity and seismic scaling in WR4. **(a)** Seismicity on the east side of WR4 where
 448 the bent segment is located (location see Figure 1c). **(b)** Moment magnitude (M_W) vs distance.
 449 The grey dots denote the full icequake dataset examined in this paper. The colored dots denote
 450 icequakes within 4 km in distance from station DR14 and $M_W > -1$. The colors in **a** and **b**
 451 represent the normalized population density of icequakes. **(c)** Gutenberg-Richter (G-R)
 452 relationship of the icequakes. The blue curve is the full dataset, whereas the red circles are the
 453 colored events in **b**. The purple and orange lines represent the least square fits to the G-R
 454 relation when M_W is smaller and greater than -0.4, respectively.



455

456

457

458

459

460

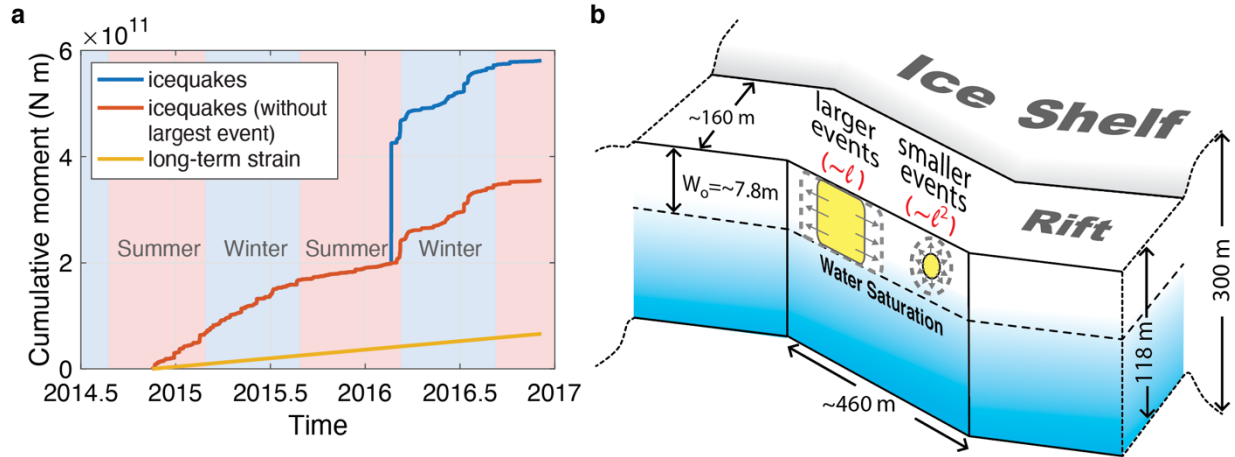
461

462

463

464

Figure 3. Surface deformation. **(a)** Principal strain rates calculated from long-term surface horizontal velocities (Figure S2). The direction of the bars indicate the principal axes orientations. **(b)** Surface displacement time series recorded from GNSS station DR10 (location see Figure 1b,c). E-W, N-S, and U-D represent east-west, north-south, and vertical displacements, respectively. Note the long-term horizontal displacement trends are removed. **(c)** Differential displacement time series between stations DR10 and DR14 (DR10 relative to DR14). The grey and red colors are the raw measurements and after 60-sample moving average, respectively. The blue vertical lines in **b** and **c** indicate individual icequake events.



465

466 **Figure 4. (a)** Cumulative icequake seismic (red and blue) moment and the strain energy due to
 467 long-term rift opening (yellow). **(b)** Conceptual model of the icequake scaling. For smaller
 468 events, slip area grows with length square (l^2), but the slip area cannot grow past W_o , the brittle-
 469 ductile transition at ~ 7.8 m depth. Slip area grows laterally with a length scale (l) for events with
 470 magnitude $M_W > -0.4$.